

Nonlinear analysis on purely mechanical stabilization of a wheeled inverted pendulum on a slope

Katsutoshi Yoshida · Munehisa Sekikawa · Kenta Hosomi

Received: 22 May 2015 / Accepted: 31 August 2015

Abstract This paper investigates the potential for stabilizing an inverted pendulum without electric devices, using gravitational potential energy. We propose a wheeled mechanism on a slope, specifically, a wheeled double pendulum, whose second pendulum transforms gravity force into braking force that acts on the wheel. In this paper, we derive steady-state equations of this system and conduct nonlinear analysis to obtain parameter conditions under which the standing position of the first pendulum becomes asymptotically stable. In this asymptotically stable condition, the proposed mechanism descends the slope in a stable standing position, while dissipating gravitational potential energy via the brake mechanism. By numerically continuing the stability limits in the parameter space, we find that the stable parameter region is simply connected. This implies that the proposed mechanism can be robust against errors in parameter setting.

Keywords Wheeled inverted pendulum · Passive control · Gravity · Friction · Asymptotic stabilization

1 Introduction

Electric and electronic control devices are indispensable for a variety of modern technologies. However, these technologies typically become useless during massive power outages such as those caused by natural

or other disasters. In this paper, we consider a non-electrified alternative control method to stabilize an inverted pendulum using gravitational potential. Our proposed mechanism is a wheeled inverted pendulum that descends a slope. The brake mechanism of our proposed mechanism transforms gravity force into friction force between the pendulum and the wheel. This friction produces a restoring force by which the pendulum is asymptotically stabilized in a standing position.

Approaches similar to ours can be found in the field of passive dynamic walking, pioneered by McGeer [1], in which two-legged mechanisms are designed to stably walk down a slope that consume only gravitational potential energy. Extensive studies have been reported on the passive dynamic walking, including experimental development of passive walkers [1–3] and nonlinear analyses of passive dynamic walking based on simplified models [4–6]. Early insights into the use of such passivity can also be found in the study of passive gravity-gradient attitude stabilization [7–10] wherein the alignment of one axis of a satellite along the earth’s local vertical direction was achieved without the use of active control elements.

On the other hand, the wheeled inverted pendulum has attracted significant attention in the fields of control engineering and robotics. Because of the applications of wheeled inverted pendulums in personal mobility devices, including the Segway[®] [11], methods for controlling wheeled inverted pendulums have been developed via approaches such as partial feedback linearization [12], inclined surface control [13], sliding-mode velocity control [14], neuro-fuzzy-based control [15], and robust control based on a quasi-linear parameter-varying model [16]. Not surprisingly, these studies implied the use of electric devices.

K. Yoshida · M. Sekikawa

Department of Mechanical and Intelligent Engineering, Utsunomiya University, 7-1-2 Yoto, Utsunomiya, Tochigi 321-8585, Japan E-mail: yoshidak@katzlab.jp

K. Hosomi

Isuzu Motors Limited, 6-26-1 Minami, Shinagawa, Tokyo 140-8722, Japan

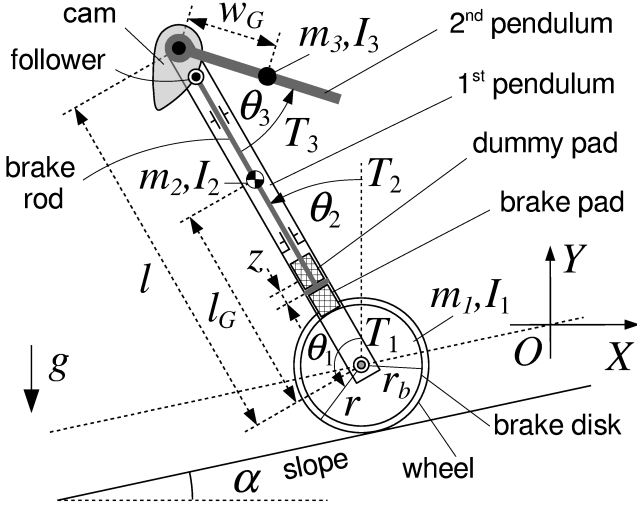


Fig. 1 Friction-controlled wheeled inverted pendulum (FCWIP).

In this paper, we merge concepts from passive dynamic walking and studies of the wheeled inverted pendulum to derive our new mechanical design for the non-electrified stabilization of a wheeled inverted pendulum. As stated above, we propose a wheeled double pendulum mechanism, whose second pendulum transforms gravity force into braking force that acts on the wheel. To investigate the dynamic stabilities of this newly proposed mechanism, we start with deriving a nonlinear analytical model of the mechanism to examine the stabilities of its steady states. Three types of critical points arise in the analytical model. These critical points are analytically characterized and numerically continued in the parameter space to obtain stability limits for the steady standing motions. It is found that the stability of the proposed mechanism is limited by Hopf bifurcation and vanishing external resistance on the wheel.

2 Wheeled inverted pendulum with friction control

We propose a wheeled inverted pendulum with friction control, as shown in Fig. 1, that comprises 1) a wheel placed on a slope without slipping, 2) a double pendulum suspended on the wheel axis, and 3) a friction control mechanism that generates a braking force on the wheel proportional to the angle between the first and second pendulums. Hereinafter, we refer to this model as a friction-controlled wheeled inverted pendulum (FCWIP).

Configuration of the FCWIP can be described by a three-dimensional generalized coordinate: (T denotes transpose)

$$\theta = (\theta_1, \theta_2, \theta_3)^T, \quad (1)$$

Table 1 Mechanical parameters of the wheeled double pendulum.

| Parameters | Values |
|------------|---|
| m_1 | mass of wheel 0.1 kg |
| m_2 | mass of 1st pendulum 0.2 kg |
| m_3 | mass of 2nd pendulum 1 kg |
| I_1 | moment of inertia of wheel $m_1 r^2/2$ kg·m ² |
| I_2 | moment of inertia of 1st pendulum $m_2 l^2/12$ kg·m ² |
| I_3 | moment of inertia of 2nd pendulum 0.25 kg·m ² |
| r | radius of wheel 0.2 m |
| l | length of 1st pendulum 1 m |
| l_G | placement of center of gravity of 1st pendulum $l/2$ |
| w | length of 2nd pendulum 0.7 m |
| w_G | placement of center of gravity of 2nd pendulum 0.6 m |
| g | acceleration of gravity 9.8 m/s ² |
| α | angle of slope 0.1 rad |

where θ_1 is the rotational angle of the wheel, θ_2 is the absolute slant angle of the first pendulum, and θ_3 is the relative angle of the second pendulum from the first pendulum. In addition, we consider the corresponding generalized force:

$$\mathbf{T} = (T_1, T_2, T_3)^T, \quad (2)$$

where T_i is a torque acting on θ_i .

2.1 Wheeled double pendulum

Unless the friction control mechanism (or \mathbf{T}) is specified, the FCWIP in Fig. 1 is simply a wheeled double pendulum whose Lagrangian is given by

$$L := T - U : \quad (3)$$

$$T := \frac{1}{2} \dot{\theta}_1^2 (Q_1 r + I_1) + \frac{1}{2} \dot{\theta}_2^2 \{-2Q_3 l \cos(\theta_3) + Q_2 + I_2\} \\ + \frac{1}{2} \dot{\theta}_3^2 (Q_3 w_G + I_3) + \dot{\theta}_2 \dot{\theta}_3 Q_3 \{w_G - l \cos(\theta_3)\} \\ + \dot{\theta}_1 \dot{\theta}_2 \{-Q_3 r \cos(\alpha - \theta_2 - \theta_3) + Q_4 r \cos(\alpha - \theta_2)\} \\ - \dot{\theta}_1 \dot{\theta}_3 Q_3 r \cos(\alpha - \theta_2 - \theta_3), \quad (4)$$

$$U := -g \{Q_3 \cos(\theta_2 + \theta_3) - Q_4 \cos(\theta_2) + \theta_1 Q_1 \sin(\alpha)\}, \quad (5)$$

with

$$Q_1 = (m_1 + m_2 + m_3)r, \\ Q_2 = m_2 l_G^2 + m_3 (w_G^2 + l^2), \\ Q_3 = m_3 w_G, \quad Q_4 = m_2 l_G + m_3 l, \quad (6)$$

where the physical parameters are listed in Table 1.

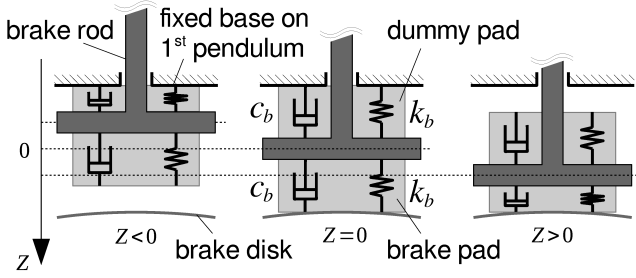


Fig. 2 Example of the structure of the brake mechanism

On substituting L into Lagrange's equations with the generalized force \mathbf{T} , we obtain the equations of the motion of the wheeled double pendulum as

$$M\ddot{\boldsymbol{\theta}} = \mathbf{F} + \mathbf{T}, \quad (7)$$

with

$$\begin{aligned} M^T &= M, \quad M_{11} = Q_1 r + I_1, \\ M_{12} &= -Q_3 r \cos(\alpha - \theta_2 - \theta_3) + Q_4 r \cos(\alpha - \theta_2), \\ M_{13} &= -Q_3 r \cos(\alpha - \theta_2 - \theta_3), \\ M_{22} &= -2Q_3 l \cos(\theta_3) + Q_2 + I_2, \\ M_{23} &= Q_3 \{w_G - l \cos(\theta_3)\}, \quad M_{33} = Q_3 w_G + I_3, \end{aligned} \quad (8)$$

and

$$\begin{aligned} F_1 &= Q_3 r (\dot{\theta}_2 + \dot{\theta}_3)^2 \sin(\alpha - \theta_2 - \theta_3) \\ &\quad - Q_4 r \dot{\theta}_2^2 \sin(\alpha - \theta_2) + g Q_1 \sin(\alpha), \\ F_2 &= -Q_3 l \dot{\theta}_3 (2\dot{\theta}_2 + \dot{\theta}_3) \sin(\theta_3) \\ &\quad - g \{Q_3 \sin(\theta_2 + \theta_3) - Q_4 \sin(\theta_2)\}, \\ F_3 &= Q_3 l \dot{\theta}_2^2 \sin(\theta_3) - g Q_3 \sin(\theta_2 + \theta_3), \end{aligned} \quad (9)$$

where M_{ij} represents the (i, j) component of the matrix M and F_i is the i th component of the vector \mathbf{F} .

2.2 Friction control mechanism

Next, we introduce a friction control mechanism (FCM) into the wheeled double pendulum by specifying \mathbf{T} as follows.

Let z be a displacement of the brake rod outputted from the cam mechanism, as shown in Fig. 1, and suppose that the cam function $z(\theta_3)$ is given as a linear function:

$$z = z(\theta_3) := \rho(\theta_3 - \eta), \quad \dot{z} = \rho \dot{\theta}_3 \quad (10)$$

where ρ is a cam ratio and $\eta > 0$ is an offset angle. Accordingly, the follower is expected to follow both the positive and negative rotation of the cam.

Then, we consider a brake mechanism, as shown in Fig. 2. In this mechanism, a pad (in light gray) is

bonded on a brake rod (in dark gray) and sandwiched between the fixed base on the first pendulum and the brake disk without clearance at $z = 0$. We refer to the lower half of the pad as a brake pad and the upper half as a dummy. The dummy pad has no function in terms of braking but is assumed to have the same mechanical property as the brake pad.

Thus, the brake pad touches the brake disk when $z \geq 0$ but is separated from the disk when $z < 0$. We assume that the brake rod receives a continuous reaction force from the pads in the following form:

$$\begin{aligned} R &= R(z, \dot{z}) := -(k_b z + c_b \dot{z}) \\ &= -\rho \{k_b(\theta_3 - \eta) + c_b \dot{\theta}_3\}, \end{aligned} \quad (11)$$

where c_b and k_b are viscoelastic coefficients of the pad.

The reaction force R produces a torque on θ_3 as a generalized force F_{θ_3} on θ_3 , given by

$$F_{\theta_3} = \frac{\partial z}{\partial \theta_3} R(z, \dot{z}) = \rho R(z, \dot{z}). \quad (12)$$

At the same time, we assume that R causes a Coulomb friction force between the brake pad and the brake disk. This force can be modeled by a tangential force on the contact surface as

$$F_R = \mu R(z, \dot{z}) \operatorname{sgn}(\dot{\theta}_1 - \dot{\theta}_2) \chi(z) \quad (13)$$

where μ is the Coulomb friction coefficient, $\operatorname{sgn}(\cdot)$ is the unit signum function, and $\chi(\cdot)$ is the unit step function representing the separation of the brake pad from the brake disk. We have the torques T_i on θ_i ($i = 1, 2, 3$) as

$$\begin{cases} T_1 = r_b F_R - c_1 |\dot{\theta}_1| \dot{\theta}_1, \\ T_2 = -r_b F_R, \\ T_3 = F_{\theta_3} = \rho R(z, \dot{z}), \end{cases} \quad (14)$$

where c_1 is the coefficient of the quadratic resistance including aerodynamic force on the wheel (or θ_1). Table 2 summarizes the parameters of the FCM and quadratic resistance. Note that the value of the spring coefficient listed in Table 2 can be obtained approximately from a medium-carbon steel rod (Young's modulus 205 GPa) of 5×10^{-4} m diameter and 0.5 m length.

Therefore, we derive the dynamic model of the FCWIP as the wheeled double pendulum in (7) with the braking torque in (14).

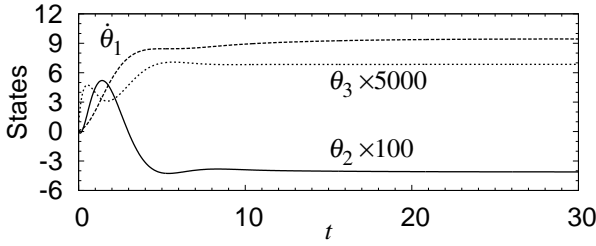
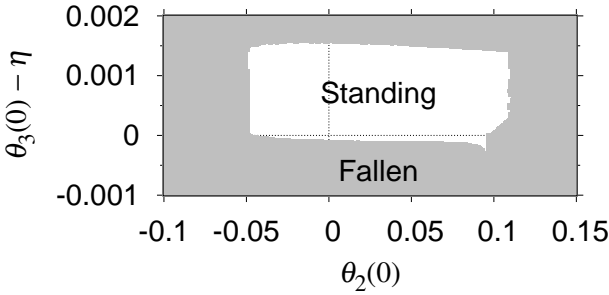
2.3 Numerical examples

Figure 3 shows a numerical solution of the FCWIP model obtained by solving (2), (7), and (14) from the trivial initial state $\theta_1(0) = \theta_2(0) = 0$, $\theta_3(0) = \eta$ (or

Table 2 Parameters of the FCM.

| Parameters | Values |
|--|------------------------------------|
| r_b radius of brake disk | 0.18 m |
| ρ cam ratio | 1/20 |
| k_b spring coefficient of the brake | 8×10^4 N/m |
| c_b viscous coefficient of the brake | $(2 \times 10^4 \text{ Ns/m})$ |
| μ Coulomb friction coefficient of the brake | (0.249) |
| η offset of the brake mechanism | $(2 \times 10^{-4} \text{ rad})$ |
| c_1 coefficient of quadratic resistance on the wheel | $(5 \times 10^{-4} \text{ Nms}^2)$ |

Parentheses around values denote nominal values.

**Fig. 3** Time responses of the FCWIP for the condition listed in Tables 1 and 2.**Fig. 4** Attraction basin of the stable steady state in Fig. 3.

$z(0) = 0$), and $\dot{\theta}_i(0) = 0$ ($i = 1, 2, 3$). The parameter values are listed in Table 1 and 2 that are empirically chosen to achieve a stable standing motion. For numerical integration, a fourth-order Runge-Kutta-Gill method is employed with a time step of 10^{-3} .

As shown in Fig. 3, the FCWIP model becomes asymptotically stable under the suitable parameter condition. In this example, the angle of the first pendulum $\theta_2(t)$ converges to a small negative value representing a standing position that is slightly slanted toward the upside of the slope. Consequently, the angle of the second pendulum $\theta_3(t)$ converges to a small positive value that represents it hanging from the first pendulum to produce the brake force F_R in (13). Moreover, the descent velocity of the wheel $\dot{\theta}_1(t)$ converges to 9.46 rad/s (6.81 km/h in translational velocity).

Figure 4 shows the sets of initial angles $\theta_2(0), \theta_3(0)$ of the first and second pendulums, respectively. The other initial values are set as $\theta_1(0) = \dot{\theta}_i(0) = 0$ ($i =$

1, 2, 3). The area hatched in gray is the set of initial angles from which the state converges to fallen positions of the FCWIP model, and the white area surrounded by the hatched area is the set that converges to the steady standing state, as shown in Fig. 3. From Fig. 4, it appears that the set of the initial angles that belongs to the standing position forms a mostly connected area. Therefore, it can be expected that the proposed FCWIP model exhibits some robustness against disturbance of the initial angles.

Considering potential real-life applications of the proposed system, dependencies of the parameters on the size of the attraction basin that belongs to the standing position could be a crucial problem. This will be addressed in a future study.

3 Steady-state analysis

3.1 State-space representation

For a simple expression, we perform a time scale transformation $t := qt^*$, where q is a time scale and t^* is nondimensional time. Taking a state vector:

$$\mathbf{x} := (\theta_1, \theta_2, \theta_3 - \eta, q\dot{\theta}_1, q\dot{\theta}_2, q\dot{\theta}_3)^T, \quad \dot{\theta}_i := d\theta_i/dt, \quad (15)$$

we transform the dynamic model (7) and (14) to a state-space form:

$$\dot{\mathbf{x}} = \mathcal{M}(\mathbf{x})^{-1} \{ \mathbf{f}(\mathbf{x}) + \boldsymbol{\tau}(\mathbf{x}) \}, \quad \dot{\mathbf{x}} := d\mathbf{x}/dt^*, \quad (16)$$

with

$$\mathcal{M}(\mathbf{x}) := \text{diag}(E_3, M(\mathbf{x})), \quad (17)$$

$$\mathbf{f}(\mathbf{x}) := \begin{pmatrix} x_4 \\ x_5 \\ x_6 \\ q^2 \mathbf{F}(\mathbf{x}) \end{pmatrix}, \quad \boldsymbol{\tau}(\mathbf{x}) := \begin{pmatrix} 0 \\ 0 \\ 0 \\ q^2 \mathbf{T}(\mathbf{x}) \end{pmatrix}, \quad (18)$$

where $M(\mathbf{x})$, $\mathbf{F}(\mathbf{x})$, and $\mathbf{T}(\mathbf{x})$ are the matrix and vectors in the dynamic model (7) and (14) via (15), and E_3 is a 3×3 identity matrix.

We choose $q := (k_b \rho^2)^{-1/2}$ to normalize the spring coefficient k_b and introduce nondimensional parameters listed in Table 3. In this case, the components of the vectors in (18) are obtained as

$$\begin{cases} q^2 F_1 = -Q_3 r (x_5 + x_6)^2 \sin(\eta + x_2 + x_3 - \alpha) \\ \quad + Q_4 r x_5^2 \sin(x_2 - \alpha) + g^* Q_1 \sin(\alpha), \\ q^2 F_2 = -Q_3 l x_6 (2x_5 + x_6) \sin(\eta + x_3) \\ \quad - g^* \{ Q_3 \sin(\eta + x_2 + x_3) - Q_4 \sin(x_2) \}, \\ q^2 F_3 = Q_3 l x_5^2 \sin(\eta + x_3) - g^* Q_3 \sin(\eta + x_2 + x_3), \end{cases}$$

Table 3 Nondimensional parameters.

| Parameters | Values | Definition |
|--------------------------------------|----------------------|-----------------------|
| q time scale | $200^{-1/2}$ | $(k_b \rho^2)^{-1/2}$ |
| k_b^* spring coefficient | 1 | $(q^2 \rho^2) k_b$ |
| g^* acceleration of gravity | 4.9×10^{-2} | $(q^2) g$ |
| μ^* Coulomb friction coefficient | (0.8964) | $(r_b \rho^{-1}) \mu$ |
| c_b^* viscous coefficient | (3.536) | $(q \rho^2) c_b$ |

The values are transformed from the original parameters in Tables 1 and 2. Parentheses around values denote nominal values.

(19)

and

$$\begin{cases} q^2 T_1 = -\mu^* \text{sgn}(x_4 - x_5) \chi(x_3) \{x_3 + c_b^* x_6\} \\ \quad - c_1 |x_4| x_4, \\ q^2 T_2 = \mu^* \text{sgn}(x_4 - x_5) \chi(x_3) \{x_3 + c_b^* x_6\}, \\ q^2 T_3 = -\{x_3 + c_b^* x_6\}. \end{cases} \quad (20)$$

3.2 Assumption of steady state

In view of the numerical example presented in Fig. 3, we consider a steady state \mathbf{x}^* of the FCWIP model (16) that satisfies

$$\dot{\mathbf{x}} = \dot{\mathbf{x}}^* := (\omega, 0, 0, 0, 0, 0)^T, \quad \omega > 0 \text{ (constant)}. \quad (21)$$

The steady state \mathbf{x}^* mentioned above describes the rotation of the wheel down the slope with a constant angular velocity $x_4^* = \omega > 0$ while the first and second pendulum maintain certain steady angles x_2^* and x_3^* , respectively, with $x_5^* = x_6^* = 0$. The angles x_2^* and x_3^* are assumed to satisfy the following conditions:

- (A) $x_2^* < 0$: the first pendulum reaches a standing position (slightly) slanted to the upside of the slope.
- (B) $x_3^* > 0$ (or $z^* > 0$): due to (A), the second pendulum hangs from the first pendulum (due to gravity and while maintaining $x_2^* < 0$) to produce the brake force F_R in (13).

These conditions are required to stabilize the first pendulum in a standing position. Because, they guarantee existence of the braking force F_R caused by a negative clearance between the brake pad and disk, $x_3^* > 0$ (or $z^* > 0$), and that is mechanically caused by $x_2^* < 0$. Otherwise, the braking force vanishes, and the FCWIP becomes nothing more than an uncontrolled wheeled double pendulum that can never be stabilized around the standing position.

In addition, note that the FCWIP model, in absence of the floor model of the slope, can theoretically have

another stable steady state, a static equilibrium where the second pendulum is hanging down at rest at $x_2^* = \pi + \epsilon_2$ and $x_3^* = \epsilon_3$ for small $\epsilon_2, \epsilon_3 > 0$.

3.3 Steady-state equation

The steady-state equation is given by

$$\dot{\mathbf{x}}^* = \mathcal{M}(\mathbf{x}^*)^{-1} \{ \mathbf{f}(\mathbf{x}^*) + \boldsymbol{\tau}(\mathbf{x}^*) \}, \quad (22)$$

where the derivative $\dot{\mathbf{x}}^*$ is the constant vector already defined in (21) and \mathbf{x}^* is an unknown vector representing the steady state. Multiplying both the sides by $\mathcal{M}(\mathbf{x}^*)$, we obtain

$$\mathbf{f}(\mathbf{x}^*) + \boldsymbol{\tau}(\mathbf{x}^*) = \mathcal{M}(\mathbf{x}^*) \dot{\mathbf{x}}^* = \text{diag}(E_3, M(\mathbf{x}^*)) \dot{\mathbf{x}}^* = \dot{\mathbf{x}}^* \quad (23)$$

where the last equality is due to the zero components of $\dot{\mathbf{x}}^* := (\omega, 0, 0, 0, 0, 0)$. Therefore, the steady-state condition is obtained as follows:

$$x_4^* = \omega, \quad x_5^* = x_6^* = 0, \quad (24)$$

$$0 = q^2 F_1 + q^2 T_1 = g^* Q_1 \sin(\alpha) - c_1 \omega^2 - \mu^* x_3^*, \quad (25)$$

$$0 = q^2 F_2 + q^2 T_2 = -g^* \{ Q_3 \sin(\eta + x_2^* + x_3^*) - Q_4 \sin(x_2^*) \} + \mu^* x_3^*, \quad (26)$$

$$0 = q^2 F_3 + q^2 T_3 = -g^* Q_3 \sin(\eta + x_2^* + x_3^*) - x_3^*, \quad (27)$$

where $|x_4^*| x_4^* = \omega^2$ and $\text{sgn}(x_4^* - x_5^*) \chi(x_3^*) = 1$ are substituted according to the assumption: $x_4^* - x_5^* = x_4^* = \omega > 0$ and $x_3^* > 0$ in Section 3.2.

Note that the equations (25), (26), and (27) represent the balance of the torque from the brake force and the gravity force at about θ_1 , θ_2 , and θ_3 , respectively. In particular, (25) can also be derived from the balance of the energy supply from the gravitational potential and the energy consumption via Coulomb friction and quadratic resistance.

The steady-state equations in (24), (25), (26), and (27) can be reduced to the following form:

$$\begin{cases} x_5^* = x_6^* = 0, \\ c_1 (x_4^*)^2 = g^* Q_1 \sin(\alpha) - \mu^* x_3^* > 0, \\ \sin(x_2^*) = -\frac{(1 + \mu^*) x_3^*}{g^* Q_4}, \\ \sin(x_2^* + x_3^* + \eta) = -\frac{x_3^*}{g^* Q_3}. \end{cases} \quad (28)$$

Thus, we have derived the steady-state equations of the FCWIP model with three unknowns x_2^* , x_3^* , and x_4^* ($= \omega$). Note that the angle of the wheel in the steady state $x_1^*(t) \propto \omega t$ never appears explicitly in these steady-state equations.

It is clear from (28) that under the given mechanical structure and environment, the nontrivial components of steady state (x_2^*, x_3^*, x_4^*) depend on three parameters, namely μ^* , η , and c_1 . More precisely, x_2^* and x_3^* can be solved independently of x_4^* , and they depend on the nondimensional friction μ^* and the offset η of the FCM. After that, x_4^* is obtained as a function of x_3^* depending on c_1 .

3.4 Jacobian matrix at steady state

We consider a variation $\delta \mathbf{x}$ of \mathbf{x} around \mathbf{x}^* as $\mathbf{x} := \mathbf{x}^* + \delta \mathbf{x}$ and substitute it into the state-space model (16) as $\mathcal{M}(\mathbf{x}^* + \delta \mathbf{x})\{\dot{\mathbf{x}}^* + \delta \dot{\mathbf{x}}\} = (\mathbf{f} + \boldsymbol{\tau})(\mathbf{x}^* + \delta \mathbf{x})$. The i th component of the left side can be written by the Einstein notation as

$$\begin{aligned} L_i &= \mathcal{M}_{ij}(\mathbf{x}^* + \delta \mathbf{x})\{\dot{x}_j^* + \delta \dot{x}_j\} \\ &= \left\{ \mathcal{M}_{ij}(\mathbf{x}^*) + \frac{\partial \mathcal{M}_{ij}}{\partial x_k} \delta x_k \right\} \{\dot{x}_j^* + \delta \dot{x}_j\} + O(\delta \mathbf{x}, \delta \dot{\mathbf{x}})^2 \\ &= \mathcal{M}_{ij}(\mathbf{x}^*)\dot{x}_j^* + \mathcal{M}_{ij}(\mathbf{x}^*)\delta \dot{x}_j \\ &\quad + \frac{\partial \mathcal{M}_{ij}}{\partial x_k} \delta x_k \dot{x}_j^* + O(\delta \mathbf{x}, \delta \dot{\mathbf{x}})^2. \end{aligned} \quad (29)$$

Due to the structures of $\mathcal{M} = \text{diag}(E_3, M)$ and $\dot{\mathbf{x}}^* = (\omega, 0, 0, 0, 0, 0)^T$, we have

$$\frac{\partial \mathcal{M}_{ij}}{\partial x_k} \delta x_k \dot{x}_j^* = 0 = \begin{cases} 0 \cdot \delta x_k \omega & (j = 1) \\ \frac{\partial \mathcal{M}_{ij}}{\partial x_k} \delta x_k \cdot 0 & (j > 1) \end{cases} \quad (30)$$

for all i and j . Therefore, neglecting the second and higher order term of $\delta \mathbf{x}$ and $\delta \dot{\mathbf{x}}$, we arrive at a variation equation of (16) as

$$\delta \dot{\mathbf{x}} = \mathcal{M}(\mathbf{x}^*)^{-1} \left\{ D\mathbf{f}(\mathbf{x}^*) + D\boldsymbol{\tau}(\mathbf{x}^*) \right\} \delta \mathbf{x} =: J(\mathbf{x}^*) \delta \mathbf{x}, \quad (31)$$

where $D\mathbf{f}(\mathbf{x}^*)$ denotes the Jacobian matrix of $\mathbf{f}(\mathbf{x})$ around \mathbf{x}^* and $J(\mathbf{x}^*)$ provides a closed-loop state matrix whose eigenvalues represent the stabilities of the FCWIP model. The components of $J(\mathbf{x}^*)$ are given by

$$D\mathbf{f}(\mathbf{x}^*) = \begin{pmatrix} 0 & 0 & 0 & 1 & 0 & 0 \\ 0 & 0 & 0 & 0 & 1 & 0 \\ 0 & 0 & 0 & 0 & 0 & 1 \\ 0 & 0 & 0 & 0 & 0 & 0 \\ 0 & g^* Q_4 C_1^* - g^* Q_3 C_2^* & -g^* Q_3 C_2^* & 0 & 0 & 0 \\ 0 & -g^* Q_3 C_2^* & -g^* Q_3 C_2^* & 0 & 0 & 0 \end{pmatrix}, \quad (32)$$

where $C_1^* := \cos(x_2^*)$, $C_2^* := \cos(x_2^* + x_3^* + \eta)$, and

$$D\boldsymbol{\tau}(\mathbf{x}^*) = \begin{pmatrix} 0 & 0 & 0 & 0 & 0 & 0 \\ 0 & 0 & 0 & 0 & 0 & 0 \\ 0 & 0 & 0 & 0 & 0 & 0 \\ 0 & 0 & -\mu^* & -2c_1 x_4^* & 0 & -c_b^* \mu^* \\ 0 & 0 & \mu^* & 0 & 0 & c_b^* \mu^* \\ 0 & 0 & -1 & 0 & 0 & -c_b^* \end{pmatrix}. \quad (33)$$

To obtain (32) and (33), $|x_4| x_4 = x_4^2$ and $\text{sgn}(x_4 - x_5) \chi(x_3) = 1$ are assumed, because $x_3(t) > 0$, $x_4(t) > 0$, and $x_4(t) - x_5(t) > 0$ hold for $x_i(t) = x_i^* + \delta x_i(t)$, $|\delta x_i(t)| \ll 1$ ($i = 1, \dots, 6$).

The results in (32) and (33) imply that the stability of the FCWIP model depends on the nondimensional viscous coefficient c_b^* in addition to the parameters μ^* , η , and c_1 that determine the steady states (x_2^*, x_3^*, x_4^*) .

In summary, we have found that under a given mechanical structure and environment,

- the steady angles (x_2^*, x_3^*) depend on (μ^*, η) ,
- the steady descent velocity x_4^* depends on (μ^*, η, c_1) , and
- the stability depends on $(\mu^*, \eta, c_1, c_b^*)$.

3.5 Eigenvalue equation

It can be proved that $\text{rank}[J(\mathbf{x}^*)] = 5 < 6 = \dim \mathbf{x}$, which follows from the assumption of the uniform motion $\dot{x}_1(t) = \omega$. Thus, the characteristic equation of $J(\mathbf{x}^*)$ is given in the following form:

$$\det(J(\mathbf{x}^*) - \lambda E_6) = \lambda h(\lambda) = 0, \quad (34)$$

$$h(\lambda) = \lambda^5 + a_1 \lambda^4 + a_2 \lambda^3 + a_3 \lambda^2 + a_4 \lambda + a_5, \quad (35)$$

where $\det(\cdot)$ denotes a determinant and E_6 is a 6×6 identity matrix. For simplicity, we refer to $h(\lambda) = 0$ as an eigenvalue equation of the FCWIP model.

Therefore, the steady state \mathbf{x}^* becomes stable if the maximal real part of the eigenvalues is negative, that is

$$\Lambda := \text{Re } \lambda_{\max} < 0, \quad \lambda_{\max} := \arg \max_{\lambda} \text{Re } (\lambda), \quad (36)$$

where λ_i ($i = 1, \dots, 5$) are the roots of $h(\lambda) = 0$.

4 Critical points of steady state

As mentioned in Section 3.4, the stabilities of the steady state \mathbf{x}^* depend on μ^* , η , c_1 , and c_b^* . Here, we provide some numerical examples of that dependency. Thus, the parameter values are set to those listed in Table 1, 2, and 3 by default unless otherwise noted.

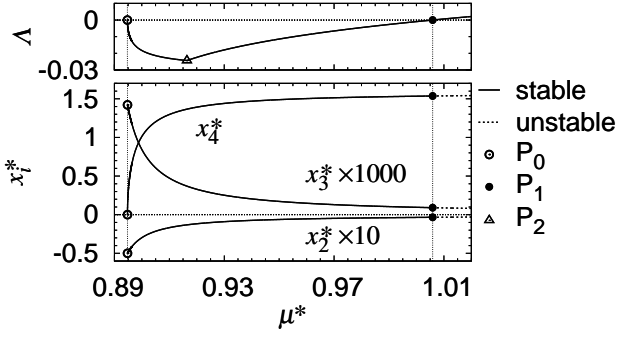


Fig. 5 Maximal real part of eigenvalue Λ and steady state x_i^* as functions of the nondimensional friction μ^* .

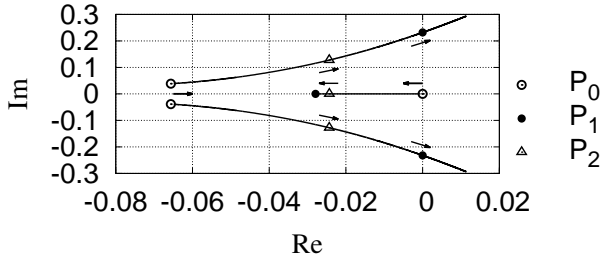


Fig. 6 Root loci along the steady states in Fig. 5.

4.1 Dependency on μ^* and η

We first examine the dependency on the nondimensional friction μ^* and the offset η , which determine the steady angles x_2^* and x_3^* via (28).

Figure 5 shows the maximal real part of the eigenvalue Λ and the nontrivial components x_i^* ($i = 2, 3, 4$) of the steady state \mathbf{x}^* as functions of the nondimensional friction μ^* . Λ and x_i^* are obtained from numerical solutions of (28) by Newton's method and (36), respectively. The solid line in the top graph represents Λ , and the solid and dotted lines in the bottom graph represent stable and unstable x_i^* , respectively. The values of x_i^* ($i = 2, 3$) are scaled to share a common vertical axis.

It is clear from Fig. 5 that three types of critical points P_0 , P_1 , and P_2 appear, which are denoted as open circles, filled circles, and a triangle, respectively. P_0 gives an infimum $\inf_{\mu^*} (x_4^*) = 0$ of the descent velocity $x_4^* > 0$, P_1 gives a stability boundary, and P_2 gives a folded (nonsmooth) minimum of $\Lambda(\mu^*)$.

To characterize these points, Fig. 6 plots the root loci of $h(\lambda) = 0$ in (35) along the steady states \mathbf{x}^* in Fig. 5. It can be numerically proven that under the considered condition, the eigenvalue equation $h(\lambda) = 0$ has three real roots and a pair of complex conjugate

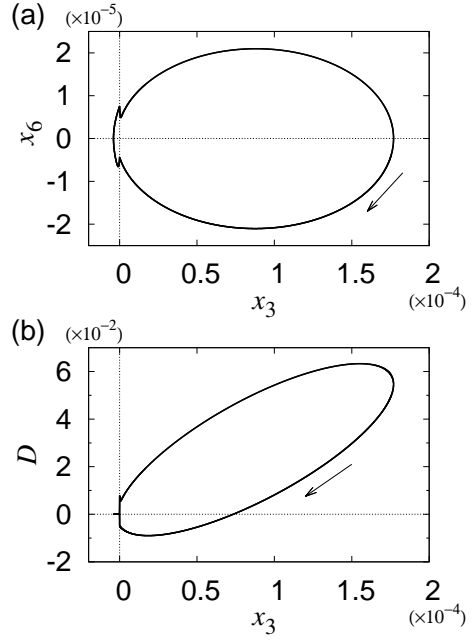


Fig. 7 Limit cycle for $\mu^* = 1.01$ (just after Hopf bifurcation).

roots as

$$\begin{aligned} \lambda_0 &= s_0, \quad \lambda_{1\pm} = s_1 \pm j\Omega, \quad \lambda_2 = s_2, \quad \lambda_3 = s_3, \\ s_0, s_1 &\gg s_2, s_3 < 0, \end{aligned} \quad (37)$$

where s_i, Ω are real numbers and $j := \sqrt{-1}$. Among the five roots, only the first three roots λ_0, λ_{1+} , and λ_{1-} affect the stability change, and only these three roots appear in the range of Fig. 6.

On the basis of the root loci obtained in Fig. 6, we can characterize the critical points in terms of eigenvalue types as follows:

- (P0): P_0 is a point such that $\lambda_{\max} = 0$.
- (P1): P_1 is a Hopf bifurcation point, for which the loci cross the imaginary axis at $\lambda_{\max} = \pm j\Omega$, where Ω is an angular frequency of a limit cycle.
- (P2): P_2 is a point such that maximal real root s_0 and the real part of the complex conjugate roots s_1 coincide, at which point they switch roles to produce the maximal real part.

Physically speaking, P_0 and P_1 provide stability limits, and P_2 maximizes the total stability or minimizes the time constant of the FCWIP model. The descent velocity vanishes ($x_4^* = 0$) at P_0 in this case, and a self-excited oscillation (limit cycle) emerges for $\Lambda(\mu^*) > 0$ near P_1 .

Figure 7 (a) shows the limit cycle for $\mu^* = 1.01$ immediately after the Hopf bifurcation point P_1 . Under this condition, the FCWIP model descends the slope in a standing position while the angles of the pendulums oscillate slightly and periodically. As this limit cycle is stable, P_1 is identified as a Hopf bifurcation point. In

general, a limit cycle occurs because of the temporal presence of negative resistance (i.e., negative energy consumption per unit time). In our problem, this is given by the braking torque T_2 in (20) multiplied by the friction velocity $(x_4 - x_5)$, specifically as

$$\begin{aligned}\mathcal{D} &= T_2 \cdot (x_4 - x_5) \\ &= q^{-2} \mu^* \text{sgn}(x_4 - x_5) \chi(x_3) (x_3 + c_b^* x_6) \cdot (x_4 - x_5) \\ &= q^{-2} \mu^* |x_4 - x_5| \chi(x_3) (x_3 + c_b^* x_6) \\ &=: C \chi(x_3) (x_3 + c_b^* x_6) \quad (C > 0),\end{aligned}\quad (38)$$

where $\text{sgn}(x)x = |x|$ is applied. As $\chi(x_3)$ is a step function, $\mathcal{D} < 0$ occurs when $x_3 \geq 0$ and $x_3 + c_b^* x_6 < 0$. This implies that when $\mathcal{D} < 0$, the brake pad (see Fig. 2 recalling $z = \rho x_3$, $\dot{z} = (\rho/q)x_6$) will be released with a velocity less than $x_6 < -x_3/c_b^* \leq 0$ while the pad is still pressed against the disk ($x_3 \geq 0$). Figure 7 (b) shows the energy consumption \mathcal{D} along the limit cycle as a function of x_3 , which numerically confirms the presence of $\mathcal{D} < 0$. During this negative energy consumption, the cycle comes across the deadband border $x_3 = z = 0$. At this point, the step function $\chi(x_3)$ jumps from 1 to 0. This causes the \mathcal{D} to jump from a negative to a positive value, similar to x_6 .

Figure 8 (a) shows the result as functions of the offset η for $\mu^* = 0.97$. In this case, a Hopf bifurcation point P_1 does not appear in the plotted range $\eta > 0$. Outside this range, x_2^* and x_3^* vanish at $\eta = 0$ and violate the physical assumptions $x_2^* < 0$ and $x_3^* > 0$ for $\eta < 0$.

4.2 Dependency on c_1 and c_b^*

Figure 8 (b) shows the results as functions of the quadratic resistance c_1 . It is clear that all the critical points P_0 , P_1 , and P_2 appear, although x_2^* and x_3^* become constant here because c_1 only affects x_4^* , as already discussed in (28).

However, the physical results of P_0 are different. That is, P_0 (or $\lambda_{\max} = 0$) on $\Lambda(\mu^*)$ in Fig. 5 corresponds to the descent velocity at rest $x_4^* = 0$. In contrast, P_0 on $\Lambda(c_1)$ in Fig. 8 (b) corresponds to the infinite descent velocity $x_4^* \rightarrow \infty$ ($c_1 \rightarrow 0$). This can be explained by the second equation in (28), which is hyperbolic with respect to c_1 and x_4^* :

$$c_1(x_4^*)^2 = g^* Q_1 \sin(\alpha) - \mu^* x_3^* \quad =: \bar{C} > 0. \quad (39)$$

This equation exhibits the following features:

- The right side of (39) (e.g., \bar{C}) is expected to be constant because x_3^* is determined independently of (39).
- The left side $c_1(x_4^*)^2$ vanishes at P_0 (or $\lambda_{\max} = 0$), as will be discussed in Section 5.1.1.

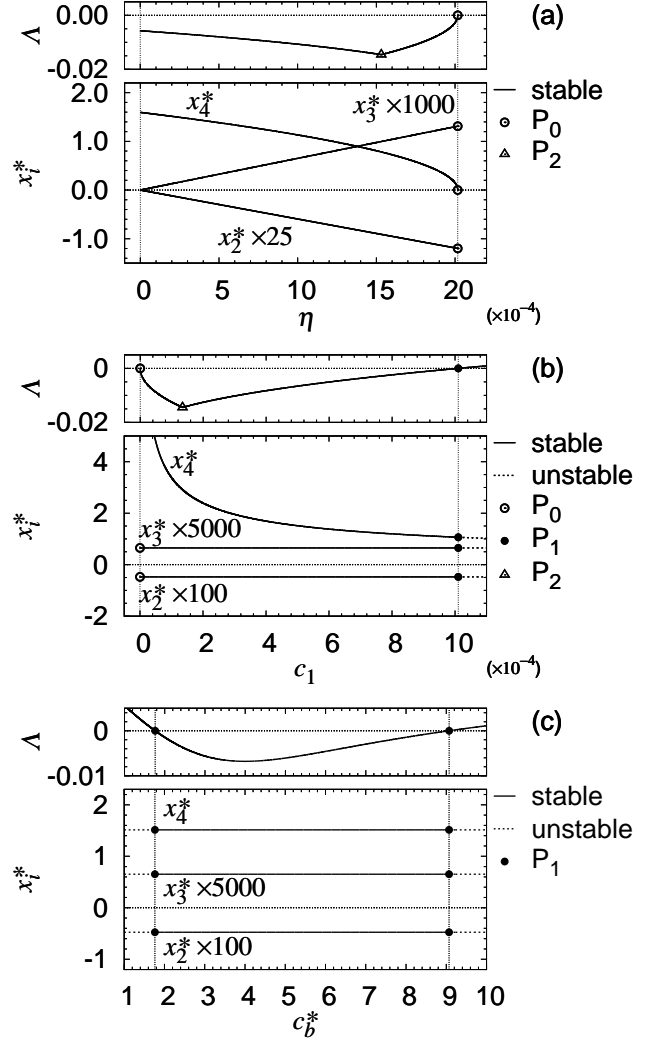


Fig. 8 Maximal real part of eigenvalue Λ and steady states x_i^* for $\mu^* = 0.97$ as functions of (a) the offset η , (b) the quadratic resistance c_1 , and (c) the viscous coefficient c_b^* .

The second feature $c_1(x_4^*)^2 = 0$ holds when $c_1 = 0$ and/or $x_4^* = 0$. The latter condition $x_4^* = 0$ directly explains P_0 in Fig. 5 for a constant $c_1 > 0$. On the other hand, P_0 in Fig. 8 (b) can be explained by the limit $c_1 \rightarrow 0$ that causes $x_4^* = \sqrt{\bar{C}/c_1} \rightarrow \infty$ for the constant \bar{C} . In addition, these different P_0 can also be explained physically. That is, the condition $c_1(x_4^*)^2 = 0$ results in vanishing of the quadratic resistance force $c_1|x_4^*|x_4^* = 0$. This can be caused by the mechanism at rest $x_4^* = 0$ as well as by the absence of the effect of the quadratic resistance $c_1 = 0$.

Figure 8 (c) plots the result for the nondimensional viscous coefficient c_b^* of the FCM. It is found that only the Hopf bifurcation point P_1 appears. Moreover, it appears that x_i^* ($i = 1, 2, 3$) are all constant because the steady-state equation in (28) is independent of c_b^* , which only

affects the components of the Jacobian matrix as $\mp c_b^* \mu^*$ and $-c_b^*$ in (33).

5 Stability limits

Finally, we numerically continue the critical points in two-parameter planes to characterize the stability limits of the FCWIP model.

5.1 Conditions of the critical points

5.1.1 Zero quadratic resistance

The condition of P_0 (or $\lambda_{\max} = 0$) is mathematically equivalent to $a_5 = 0$ in the eigenvalue equation (35). It follows that

$$\begin{aligned} 0 &= a_5 = \det \mathcal{M}^{-1} \cdot 2c_1 x_4^* g^* \\ &\quad \times \left\{ -C_1^* Q_4 - C_2^* Q_3 \{C_1^* g^* Q_4 - (1 + \mu^*)\} \right\} \\ \iff 0 &= c_1 x_4^* \left\{ C_1^* Q_4 + C_2^* Q_3 \{C_1^* g^* Q_4 - (1 + \mu^*)\} \right\} \\ \iff c_1 x_4^* &= 0 \\ \iff c_1 = 0 \text{ or } x_4^* = 0 &\iff c_1 (x_4^*)^2 = 0. \end{aligned} \quad (40)$$

Therefore, it is mathematically shown that the sufficient condition for P_0 (or $\lambda_{\max} = 0$) is given by the zero quadratic resistance $c_1 (x_4^*)^2 = 0$.

As discussed in Section 4.2, the condition P_0 (or $c_1 (x_4^*)^2 = 0$) causes two distinct descent velocities: $x_4^* = 0$ for $c_1 > 0$ and $x_4^* = \infty$ for $c_1 = 0$. Therefore, we denote them as P_0^0 and P_0^∞ , respectively, in the following sections.

The condition of P_0^0 is given by (39) with $c_1 (x_4^*)^2 = 0$, from which we can eliminate x_2^* and x_3^* to obtain

$$\begin{aligned} \Phi_0 := \eta + \arcsin \left(\frac{Q_1 \sin \alpha}{Q_3 \mu^*} \right) + \frac{g^* Q_1 \sin \alpha}{\mu^*} \\ - \arcsin \left(\frac{Q_1 (1 + \mu^*) \sin \alpha}{Q_4 \mu^*} \right) = 0. \end{aligned} \quad (41)$$

On the other hand, P_0^∞ is simply given by $c_1 = 0$. Because the condition (41) does not contain x_2^* and x_3^* , the zero quadratic resistance points P_0^0 and P_0^∞ are determined independently of the pendulum angles x_2^* and x_3^* .

5.1.2 Hopf bifurcation

The condition P_1 (or $\lambda_{\max} = \pm j\Omega$) for a Hopf bifurcation point is given by $\text{Re } h(j\Omega) = \text{Im } h(j\Omega) = 0$. On

eliminating Ω from them, we obtain

$$\begin{aligned} \Phi_1 := a_5 \left\{ a_4 (-a_1 a_2 a_3 + a_3^2 + a_1^2 a_4) \right. \\ \left. + (-a_2 a_3 + a_1 (a_2^2 - 2a_4)) a_5 + a_5^2 \right\} = 0 \end{aligned} \quad (42)$$

for the Hopf bifurcation point. It is implied from (42) that P_1 coincides with P_0^0 (or P_0^∞) because $a_5 = 0$ for P_0^0 (or P_0^∞) leads to $\Phi_1 = 0$.

Note that, rigorously speaking, the above condition provides only a necessary condition of a Hopf bifurcation point; however, it leads to satisfactory results in the present analysis.

5.1.3 Minimal time constant

We numerically detect the condition of P_2 for the minimal time constant that satisfies

$$|s_0 - s_1| < 10^{-9} \quad (43)$$

where s_0 is the maximal real eigenvalue and s_1 is the real part of the complex conjugate eigenvalues, as defined in (37). In numerical calculations, the parameter values considered are swept to detect a point that satisfies (43), where the point in the first detection is taken as the point detected.

Note that we attempted to derive an equation for the minimal time constant in a closed form of a_1, \dots, a_5 based on a given form of eigenvalue equation: $h(\lambda) = (\lambda - \lambda_{\max})(\lambda - \lambda_{\max} - jv)(\lambda - \lambda_{\max} + jv)(\lambda^2 + p\lambda + q)$, however, the result was very weak to detect P_2 precisely. Therefore, in this paper, we employ the numerical method mentioned above, although another approach would be possible for an analytical expression of P_2 .

5.2 Numerical continuation of the critical points

Figure 9 plots the sets of the critical points P_0^0 , P_1 , and P_2 on two-parameter planes obtained from the numerical solutions of (41), (42), and (43) under (28). The results on the (μ^*, η) , (μ^*, c_1) , and (μ^*, c_b^*) planes are labeled (a), (b), and (c) respectively in Fig. 9. The solid line denotes the set of the zero quadratic resistance point P_0^0 for $x_4^* = 0$, the dotted line denotes the set of the Hopf bifurcation point P_1 , and the chained line denotes the set of the minimal time constant point P_2 . The plots of P_0^∞ for $c_1 = 0$ do not appear in the ranges of these plots. The hatched areas represent the stable regions of the steady state satisfying $\Lambda < 0$ in (36).

It is clearly seen in Fig. 9 that the stable regions are bounded by P_0^0 and P_1 and that the minimal time constant point P_2 is sandwiched between them. Note

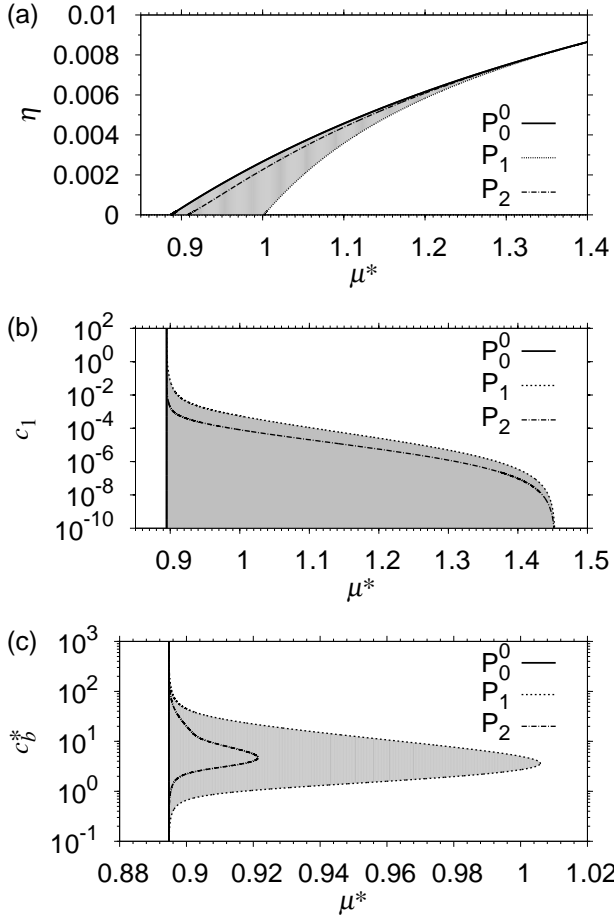


Fig. 9 Continuation of the critical points P_0^0 , P_1 , and P_2 on the two-parameter planes: (a) for the (μ^*, η) plane, (b) for the (μ^*, c_1) plane, and (c) for the (μ^*, c_b^*) plane. The hatched areas represent asymptotically stable conditions of the steady states.

that in Fig. 9 (a), the plots are bounded by the assumption $\eta > 0$ and that in Fig. 9 (b) and (c), P_0^0 lies along the vertical line at $\mu^* = \bar{\mu}^* \approx 0.89474$. This is because P_0^0 is determined independently of c_1 and c_b^* in (41). Moreover, it appears that the critical points P_0^0 , P_1 , and P_2 tend to coincide as μ^* increases on the (μ^*, η) plane, as c_b^* increases and decreases on the (μ^*, c_b^*) plane, and as c_1 increases on the (μ^*, c_1) plane. In contrast, as c_1 decreases on the (μ^*, c_1) plane, P_1 and P_2 also tend to coincide but they approach $c_1 = 0$ or P_0^∞ instead of P_0^0 . As discussed in Section 5.1.2, the convergence between P_0^0 (or P_0^∞) and P_1 can be explained by (42), in which the condition $\Phi_1 = 0$ for the Hopf bifurcation point P_1 contains $a_5 = 0$ for the zero quadratic resistance point P_0^0 (or P_0^∞). As shown in Fig. 10, however, it can be numerically proven that a purely imaginary eigenvalue $\lambda_{\max} = j\Omega$ along P_1 does not vanish even when P_1 coincides with P_0^0 (or P_0^∞) in the parameter planes. Therefore, the Hopf bifurcation point P_1 does

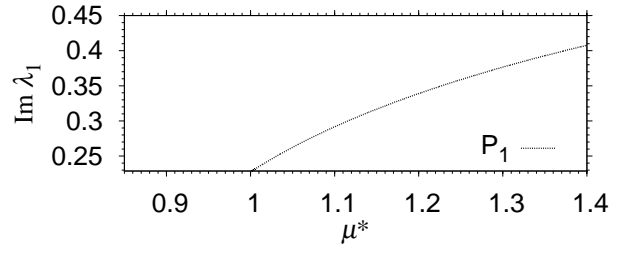


Fig. 10 Imaginary part of complex conjugate eigenvalues along P_1 in Fig. 9 (a).

not degenerate and double-zero eigenvalues never arise at that point.

From an engineering viewpoint, the results obtained above imply that the FCWIP model allows a certain amount of tolerance in parameter settings because the stable conditions are obtained as simply connected finite areas. This suggests the possibility that the proposed mechanism can work even if there are some manufacturing errors. Furthermore, the stable area on the (μ^*, η) plane in Fig. 9 (a) forms a monotonically increasing shape, which implies that the offset η can be designed to shift the stable range of the friction coefficient μ^* .

5.3 Numerical evaluation of the descent velocity

In view of engineering applications, the descent velocity (or angular velocity of the wheel) x_4^* must be adjusted to a value suitable for the intended use. Figure 11 shows the values of x_4^* mapped into a gray scale within the stable areas on the parameter planes in Fig. 9. x_4^* values are numerically obtained by solving (28).

It is clear from Fig. 11 that x_4^* tends toward zero as the parameter conditions approach P_0^0 (solid lines), which is in agreement with the definition of P_0^0 . Especially, in Fig. 11 (b), it is also clarified that x_4^* is diverging as the condition approaches P_0^∞ or $c_1 = 0$. Moreover, it appears that x_4^* changes smoothly and monotonically with the variations of the parameters. This suggests that one can adjust the descent velocity x_4^* by continuously shifting the parameters. However, it is also observed in Fig. 11 (b) that a sufficiently large value of the quadratic resistance c_1 is required to stabilize the mechanism because although a range of μ^* exists for small x_4^* near $\mu^* = \bar{\mu}^* \approx 0.89474$, it narrows significantly as c_1 decreases. In addition, it appears in Fig. 11 (c) that x_4^* does not depend on c_b^* , as discussed in the last paragraph in Section 3.4.

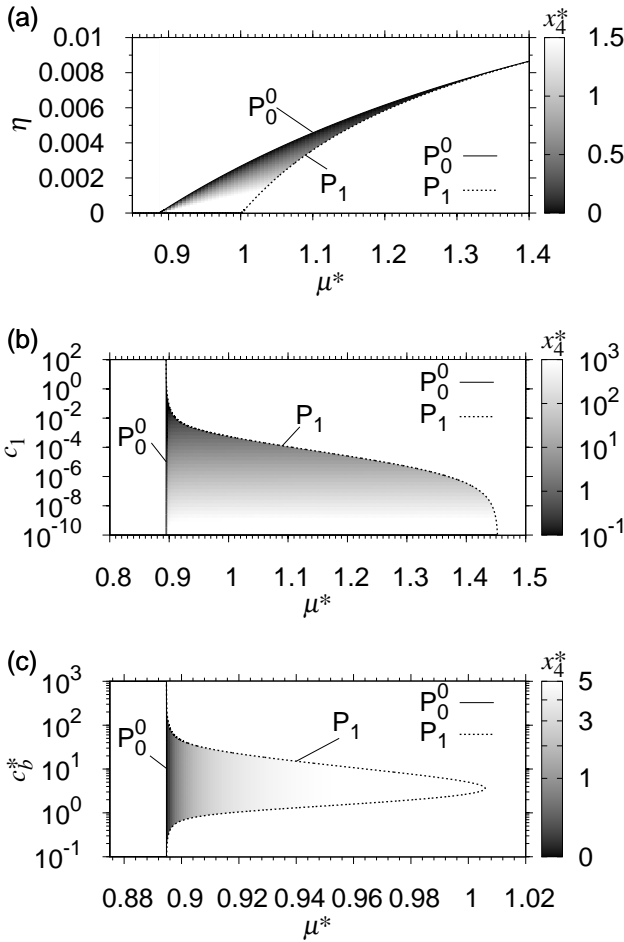


Fig. 11 Angular velocities of the wheel x_4^* within the stable areas on the two-parameter planes: (a) for the (μ^*, η) plane; (b) for the (μ^*, c_1) plane; and (c) for the (μ^*, c_b^*) plane.

6 Conclusion

For a non-electrified method to stabilize a wheeled inverted pendulum descending a slope, we proposed the FCWIP mechanism, a wheeled double pendulum, whose second pendulum transforms gravity force into brake force acting on the wheel. We conducted steady-state analysis of the proposed model and obtained the following results:

- The steady angles (x_2^*, x_3^*) depend on (μ^*, η) .
- The steady descent velocity x_4^* depends on (μ^*, η, c_1) .
- The stability depends on $(\mu^*, \eta, c_1, c_b^*)$.

Then, we found three types of critical points in the steady states, as

- P_0 : the point for zero quadratic resistance on the wheel. (P_0^0 for $x_4^* = 0$ and P_0^∞ for $x_4^* = \infty$ in detail)
- P_1 : the Hopf bifurcation point.
- P_2 : the point for the minimal time constant.

Finally, we conducted numerical continuations of these points on the two-parameter planes and evaluated the descent velocity to obtain the following results:

- The stable conditions are obtained as simply connected finite areas on the parameter planes, bounded by P_0^0 and P_1 .
- The minimal time constant point P_2 is sandwiched between P_0^0 and P_1 .
- The descent velocity x_4^* changes smoothly and monotonically with the parameter variations.

The abovementioned results lead to the conclusion that the parameter selection to design the FCWIP mechanism stabilized on a slope will not be highly sensitive, at least in theory.

In future work, we plan to develop a physical FCWIP mechanism. For this purpose, we will introduce stick-slip effects into the friction term in our model and investigate the effect on the stabilities. We also plan to conduct stochastic analysis on the FCWIP model to consider robustness against random disturbances and random parameter fluctuations.

Acknowledgements This work was supported in part by grants from the ZERO Design Project of Utsunomiya University (a project seeking novel engineering designs robust against massive outages of power, water, logistics, etc.).

References

1. McGeer, T.: Passive Dynamic Walking. *The International Journal of Robotics Research* **9**(2), 62–82 (1990)
2. Ikemata, Y., Sano, A., Yasuhara, K., Fujimoto, H.: Dynamic effects of arc feet on the leg motion of passive walker. In: 2009 IEEE International Conference on Robotics and Automation, pp. 2755–2760. IEEE (2009)
3. Coleman, M., Ruina, A.: An Uncontrolled Walking Toy That Cannot Stand Still. *Physical Review Letters* **80**(16), 3658–3661 (1998)
4. Garcia, M., Chatterjee, A., Ruina, A., Coleman, M.: The simplest walking model: stability, complexity, and scaling. *Journal of biomechanical engineering* **120**(2), 281–288 (1998)
5. Goswami, A., Thuilot, B., Espiau, B.: A study of the passive gait of a compass-like biped robot symmetry and chaos. *The International Journal of Robotics Research* **17**(12), 1282–1301 (1998)
6. Hirata, K.: On Internal stabilizing mechanism of passive dynamic walking. *SICE Journal of Control, Measurement, and System Integration* **4**(1), 29–36 (2011)

7. Black, H. D.: A passive system for determining the attitude of a satellite. *AIAA Journal* **2**(7), 1350–1351 (1964)
8. Fischell, R. E.: Passive Gravity-Gradient Stabilization for Earth Satellites. *Applied Mathematics and Mechanics*, vol. 7. Elsevier, 13–30 (1964)
9. He, C., Liu, G., Yang, L., Tian, Y.: On the passive stabilization of the equilibrium state of Lagrangian systems. *Acta Mechanica* **134**(1-2), 17–26 (1999)
10. Peiffer, K., Savchenko, A.: On Passive Stabilization in Critical Cases. *Journal of Mathematical Analysis and Applications* **244**(1), 106–119 (2000)
11. Ulrich, K.T.: Estimating the technology frontier for personal electric vehicles. *Transportation Research Part C: Emerging Technologies* **13**(5-6), 448–462 (2005)
12. Pathak, K., Franch, J., Agrawal, S.K.: Velocity and Position Control of a Wheeled Inverted Pendulum by Partial Feedback Linearization. *IEEE Transactions on Robotics* **21**(3), 505–513 (2005)
13. Kim, Y., Kim, S.H., Kwak, Y.K.: Dynamic Analysis of a Nonholonomic Two-Wheeled Inverted Pendulum Robot. *Journal of Intelligent and Robotic Systems* **44**(1), 25–46 (2006)
14. Huang, J., Zhi-Hong, G., Matsuno, T., Fukuda, T., Sekiyama, K.: Sliding-Mode Velocity Control of Mobile-Wheeled Inverted-Pendulum Systems. *IEEE Transactions on Robotics* **26**(4), 750–758 (2010)
15. Su, K., Chen, Y., Su, S.: Design of neural-fuzzy-based controller for two autonomously driven wheeled robot. *Neurocomputing* **73**(13-15), 2478–2488 (2010)
16. Vermeiren, L., Dequidt, A., Guerra, T.M., Rago-Tirmant, H., Parent, M.: Modeling, control and experimental verification on a two-wheeled vehicle with free inclination: An urban transportation system. *Control Engineering Practice* **19**(7), 744–756 (2011)